Chien Ing Yeo, Yee Seng Tan, Wai Kit Tang and Edward R.T. Tiekink*

Conformational polymorphism in a mononuclear phosphanegold(I) thiocarbamato species, $Cy_3PAu[SC(OEt)=N(C_6H_4Cl\text{-}3)]$

https://doi.org/10.1515/zkri-2024-0124
Received December 18, 2024; accepted February 12, 2025;
published online March 31, 2025

Abstract: Two polymorphs of $Cy_3PAu[SC(OEt)=N(C_6H_4Cl\text{-}3)]$, that is a triclinic form ($P\bar{1}$ with Z' = 1; the **α**-form) and a monoclinic form ($P2_1/c$; Z' = 1; the **β**-form) have been characterised. The molecular structures feature linear P–Au–S coordination geometries with close intramolecular Au···O(ethoxy) contacts of 3.1552(17) and 3.097(2) Å for the **α**- and **β**-forms, respectively. The major conformational differences between the polymorphs relates to the relative orientations of the thiocarbamato anions and of the cyclohexylphosphane ligands. Computational chemistry shows the molecular structures to be isoenergetic (single-point calculations) and to have practically a zero barrier to interconversion. An analysis of the molecular packing highlights the importance of cyclohexyl-C–H···S(thiolate) and methyl-C–H···π(chlorophenyl) contacts in the crystal of the **α**-form, and methyl-C–H···π(chlorophenyl) and π(chlorophenyl)···π(chlorophenyl) contacts in the packing of the **β**-form. While similarities are apparent in the solid-state luminescence spectra, different electronic transitions are responsible for the spectroscopic observations.

Keywords: crystal structure; polymorphism; supramolecular chemistry; Hirshfeld surface analysis; solid-state luminescence; computational chemistry

1 Introduction

The original interest in phosphanegold(I) thiocarbamato species, that is, molecules having the general formula $R_3PAu[SC(OR')=NR'']$, for R/R′/R″ = alkyl/aryl, related to their putative biological properties. Thus, the pharmacological potential of these molecules has been evaluated in the context of cancer[1–3] and microbes.[4,5] This practical interest has been supported by crystallographic studies for unambiguous structural characterisation. Indeed, the relative ease of crystallisation of these molecules has enabled some systematic studies delineating molecular packing preferences[6,7] and correlations with solid-state luminescence.[8] During these studies, instances of conformational polymorphism have arisen, that is, where one or more of the phosphane and thiocarbamato residues exhibit distinctive conformations.[9–12]

The phenomenon of polymorphism is well documented and has an enormous impact upon the pharmaceutical and several other industries.[13–19] Polymorphs can exhibit quite distinctive packing arrangements for molecules resulting in specific physiochemical properties: the discovery of a new polymorph with favourable characteristics, for example, the histamine-2 blocker Zantac® (Ranitidine Hydrochloride),[20–22] or even the intriguing “disappearing polymorph” phenomenon,[23–25] for example, the protease inhibitor Ritonavir®,[26–28] can have considerable ramifications for intellectual property issues.[29–37] The difficulty with polymorphism is highlighted by computational chemistry studies which show the energy differences between polymorphs can be rather small, with the majority of polymorphs differing in lattice energy by less than 6 kJ/mol,[38–48] which provides a rationale for concomitant crystallisation[49] whereby polymorphs can precipitate from the same solution concomitantly, an area still attracting considerable attention.[50–54]

Given the interest in the biological properties of $R_3PAu[SC(OR')=NR'']$ and related binuclear species, these molecules have been characterised in over 80 crystal structures included in the Cambridge Structural Database (CSD),[55] which was searched employing standard procedures.[56] The overwhelming majority of molecules adopt structures related to the generic structure shown in Figure 1a, where the gold atom is coordinated in a linear fashion by the phosphane-P and thiolate-S atoms, with the thiocarbamato ligand orientated to place the alkoxy-O atom in close proximity to the gold atom. Among the structures of $R_3PAu[SC(OR')=NR'']$ deposited in the CSD, there are only three pairs of polymorphs, all of which may be classified as conformational polymorphs.

***Corresponding author: Edward R.T. Tiekink**, Department of Chemistry, Universitat de les Illes Balears, Crta de Valldemossa km 7.5, 07122 Palma de Mallorca, Spain, E-mail: edward.tiekink@uib.es
Chien Ing Yeo and Yee Seng Tan, Sunway Biofunctional Molecules Discovery Centre, School of Medical and Life Sciences, Sunway University, Bandar Sunway 47500, Selangor Darul Ehsan, Malaysia
Wai Kit Tang, Department of Chemistry, Universiti Malaya, Kuala Lumpur 50603, Malaysia

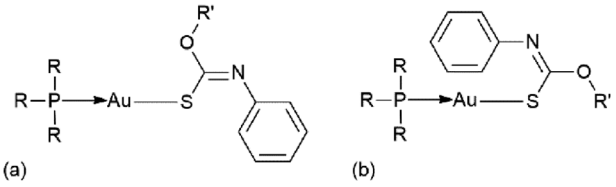

Figure 1: Chemical diagrams for the conformational polymorphs for $R_3PAu[SC(OR')=NPh]$.

For the triclinic ($P\bar{1}$)[57] and monoclinic ($P2_1/n$)[58] polymorphs of $Ph_3PAu[SC(OMe)=N(C_6H_4Cl\text{-}3)]$, the thiocarbamato ligand is orientated, as in Figure 1a, but adopt quite different conformations with respect to the Ph_3PAu residue. The remaining pairs of polymorphs reflect the carbophilic nature of gold,[59–62] whereby the thiocarbamato-phenyl rings interact weakly with the gold centre to form a stabilising interaction in one polymorphic form, akin to the orientation illustrated in Figure 1b, and with the thiocarbamato-O atom close to the gold atom in the other form, as in Figure 1a. The well recognised carbophilic nature of gold is a trait clearly of importance to the burgeoning field of gold catalysis.[63–68] In keeping with the fashion where intermolecular interactions are classified in terms of the Group of the Periodic Table the element belongs to[69–71] and which often rely on the σ-/π-hole concept of non-covalent bonding,[72–79] Au···π(C) interactions are now incorporated under the aegis "regium-bonding" which also includes interactions involving the lighter coinage elements, that is, copper and silver.[80–83]

Thus, over 20 years since the initial report of monoclinic ($P2_1/n$) $Ph_3PAu[SC(OEt)=NPh]$,[84] which adopts the motif shown in Figure 1a, a second monoclinic ($P2_1/c$) polymorph was characterised[85] which exhibits the motif shown in Figure 1b, that is, with an intramolecular Au···π(phenyl) interaction. Experiments showed the conformation with an intramolecular Au···O interaction was the kinetic outcome of crystallisation and that with the Au···π contact, the thermodynamic outcome.[85] Computational chemistry indicates the intramolecular Au···π contact is over 20 kJ/mol more stabilising than that with the Au···O interaction.[85,86] The final pair of monoclinic polymorphs, that is, with formula $(4\text{-tolyl})_3PAu[SC(OEt)=N(C_6H_4NO_2\text{-}4)]$, exhibit similar behaviour with an intramolecular Au···O interaction found in the $P2_1/c$ form[87] and a Au···π contact in the Cc form.[88]

In continuation of structural studies on this class of compound, which have shown some interesting crystallographic phenomena over the years,[6–8] the title compound was synthesised, being motivated by the desire to expand the range of substitution patterns in the N-bound substituents of the thiocarbamato anions and the relationship between this and anti-cancer and anti-microbial activity, herein is reported the crystal and molecular structures of two polymorphs of the formula $Cy_3PAu[SC(OEt)=N(C_6H_4Cl\text{-}3)]$, an analysis of the molecular packing including an evaluation of the calculated Hirshfeld surfaces as well as computational chemistry.

2 Materials and methods

2.1 Chemicals and instrumentation

All solvents were obtained from Merck and used as supplied. The chemicals were used as received without further purification: tricyclohexylphosphane (Aldrich), potassium tetrachloridoaurate(III) (Acros Organic), 3-chlorophenyl isothiocyanate (Merck), sodium sulphite (Merck) and sodium hydroxide (Merck). The ligand, $EtOC(=S)N(H)C_6H_4Cl\text{-}3$, was prepared by reacting 3-chlorophenyl isothiocyanate with ethanol in the presence of base. Tricyclohexylphosphanegold(I) chloride was prepared from the reduction of potassium tetrachloroaurate(III) by sodium sulphite followed by the addition of a molar equivalent of tricyclohexylphosphane.

The melting points were determined on a Stuart melting point apparatus SMP30 (Cole-Parmer, Chicago, USA). The ^1H and $^{13}C\{^1H\}$ NMR spectra were recorded in $CDCl_3$ solution on a Bruker Ascend 400 MHz NMR spectrometer (Bruker, Billerica, MA, USA) with chemical shifts relative to tetramethylsilane. The $^{31}P\{^1H\}$ NMR spectra were recorded in $CDCl_3$ solution on the same instrument with the chemical shifts recorded relative to 85 % aqueous H_3PO_4 as external reference; abbreviations for NMR assignments: *br*, broad; *d*, doublet; *t*, triplet; *q*, quartet; *m*, multiplet. The IR spectra were measured on a Bruker Vertex 70v FTIR spectrophotometer (Bruker, Billerica, MA, USA) from 4,000 to 400 cm^{-1}; abbreviations: *s*, strong; *m*, medium. The elemental analyses were performed on a Leco TruSpec Micro CHN Elemental Analyser (Leco, Saint Joseph, MI, USA). The luminescence spectra of solid samples were recorded on a JASCO FP-8600 spectrofluorometer (JASCO Corporation, Tokyo, Japan) equipped with liquid nitrogen cooled 100 mm ϕ integrating sphere. The low-temperature luminescent measurements were carried out on powdered samples immersed in a liquid nitrogen bath with constant flush of dried N_2. The powder X-ray diffraction (PXRD) measurements were performed on a Rigaku SmartLab with CuKα1 radiation (λ = 1.54060 Å) in the 2θ range from 5 to 40° with a step size of 0.010°. The experimental PXRD patterns were compared to the simulated PXRD patterns calculated from the respective Crystallographic Information File (CIFs) using the Rigaku PDXL2 structure analysis software package.

2.2 Synthesis and characterisation

Synthesis of $Cy_3PAu[SC(OEt)=N(C_6H_4Cl\text{-}3)]$, **1**: Sodium hydroxide (0.5 mmol, 0.020 g) in water (1 ml) was added to a suspension of tricyclohexylphosphanegold(I) chloride (0.5 mmol, 0.256 g) in acetonitrile (10 ml) followed by the addition of $EtOC(=S)N(H)C_6H_4Cl\text{-}3$ (0.5 mmol, 0.108 g) in dichloromethane (10 ml). After 3 h stirring at room temperature, the resulting mixture was left for slow evaporation at room temperature, yielding fine needles (**β**-form of **1**) after 3 weeks.

Yield: 0.249 g, 72 %. M.pt: 436.9–437.2 K. Anal. Calc'd for $C_{27}H_{42}AuClNOPS$: C, 46.86; H, 6.12; N, 2.02. Found: C, 46.48; H, 6.14; N, 2.13 %. FTIR (cm^{-1}): 1,577 (*s*) *ν*(C=N), 1,149 (*s*) *ν*(C–O), 1,087 (*m*) *ν*(C–S). ^1H NMR {$CDCl_3$}: *δ* 7.17 (*t*, 1H, aryl-H_5, J_{HH} = 7.77 Hz), 6.95–6.93 (*m*, 2H, aryl-$H_{2,4}$), 6.81 (*d*, 1H, aryl-H_6, J_{HH} = 7.80 Hz), 4.30 (*q*, 2H, OCH_2, J_{HH} = 6.94 Hz), 2.02–1.21 (*m*, *br*, 33H, Cy_3P), 1.31 (*t*, 3H, CH_3, J_{HH} = 7.13 Hz) ppm. $^{13}C\{^1H\}$ NMR {$CDCl_3$}: 165.5 (C_q), 152.3 (aryl-C_1), 133.8 (aryl-C_3), 129.4 (aryl-C_5), 122.5 (aryl-C_4), 122.3 (aryl-C_2), 120.6 (aryl-C_6), 63.7 (OCH_2), 33.3 (*d*, 1-PC_6H_{11}, J_{CP} = 27.98 Hz), 30.7 (*s*, 2-PC_6H_{11}), 27.0 (*d*, 3-PC_6H_{11}, J_{CP} = 12.07 Hz), 25.9 (*d*, 4-PC_6H_{11}, J_{CP} = 0.95 Hz), 14.6 (CH_3) ppm. $^{31}P\{^1H\}$ NMR {$CDCl_3$}: 56.8 ppm. The original spectra are given in Supplementary Materials Figure S1 (IR) and Figure S2 (^1H, $^{13}C\{^1H\}$ and $^{31}P\{^1H\}$ NMR).

2.3 Polymorph screening

Compound **1** was recrystallised from six solvent systems, that is, acetonitrile/chloroform (1:1 v/v), acetonitrile/dichloromethane (1:1 v/v), dichloromethane/ethanol (1:1 v/v), dichloromethane/isopropanol (1:1 v/v), chloroform/ethanol (1:1 v/v) and ethanol. From these trials, the **α**-form of **1** was obtained from the slow evaporation of **1** from its ethanol solution (M.pt: 437.1–437.4 K); the **β**-form of **1** was recovered from the remaining solutions. The obtained powders from each recrystallisation were subjected to PXRD analysis; the measured powder patterns were compared with the pattern generated from the respective CIF file for each of the **α**-and **β**-forms of **1**.

2.4 X-ray crystallography

The X-ray intensity data for colourless crystals of the **α**-and **β**-forms of **1** were measured at T = 100 K on a Rigaku/Oxford Diffraction XtaLAB Synergy (Dualflex, AtlasS2) diffractometer (Rigaku Oxford Diffraction, Oxford, UK) fitted with CuKα radiation (*λ* = 1.54178 Å). CrysAlisPro (Oxfordshire, England)[89] was employed for data reduction, including gaussian absorption corrections. The structures were solved by dual space direct methods using SHELXT[90] and refined (anisotropic displacement parameters and C-bound H atoms in the riding model approximation) on F^2.[91] A weighting scheme of the form $w = 1/[\sigma^2(F_o^2) + (aP)^2 + bP]$, where $P = (F_o^2 + 2F_c^2)/3$), was introduced in each case. The molecular structure diagrams were generated with ORTEP for Windows[92] with 50 % displacement ellipsoids, and the packing diagrams were drawn with DIAMOND.[93] The residual electron density peaks for the **α**-form were near the Au atom while those for the **β**-form were in the vicinity of the chlorophenyl ring. Additional data analysis was made with PLATON.[94] Crystal data and refinement details are given in Table 1.

Table 1: Crystallographic data and refinement details for the **α**- and **β**-forms of **1**.

Polymorph	α	β
Formula	$C_{27}H_{42}AuClNOPS$	$C_{27}H_{42}AuClNOPS$
Molecular weight	692.06	692.06
Crystal size/mm^3	0.06 × 0.13 × 0.30	0.14 × 0.18 × 0.28
Colour	Colourless	Colourless
Crystal system	Triclinic	Monoclinic
Space group	$P\bar{1}$	$P2_1/c$
a/Å	7.6146(1)	12.1412(1)
b/Å	13.3443(2)	18.9285(1)
c/Å	14.6344(2)	12.8511(1)
α/°	103.294(1)	90
β/°	101.583(1)	107.192(1)
γ/°	92.658(1)	90
V/Å^3	1,411.01(3)	2,821.41(4)
Z	2	4
D_c/g cm^{-3}	1.629	1.629
μ/mm^{-1}	12.037	12.040
Measured data	35,698	37,207
θ range (100 % compl.)/°	3.2–67.7	3.8–67.7
Unique data	5,813	5,837
Observed data ($I \geq 2.0\sigma(I)$)	5,777	5,808
No. parameters	299	299
R, obs. data; all data	0.021; 0.021	0.024; 0.024
a; *b* in weighting scheme	0.035; 0.698	0.025; 6.181
R_w, obs. data; all data	0.055; 0.055	0.059; 0.059
Range of residual electron density peaks/eÅ^{-3}	−1.46–+1.07	−1.39–+1.52
CCDC deposition number	2411162	2411163

2.5 Computational details

The molecular geometries of polymorphs **α** and **β** were optimised in the framework of density functional theory (DFT) at the M06 level of theory.[95] A pruned super-fine integral grid (175, 974) was used for all calculations. All

atoms were described by the Pople-type 6–311 ++ G(d,p) basis set. The harmonic frequency analyses were performed on all optimised geometries to confirm that the structures had converged to local minima on the potential energy surface (PES). The relative enthalpies were calculated and corrected by zero-point vibration energies (ZPVE). The TD-DFT calculations were also performed on the M06 optimised structure at the PBE0 level of theory[96] to obtain their absorption spectra. All DFT calculations were performed using the Gaussian 16 software package.[97]

3 Results and discussion

3.1 Isolation and spectroscopic characterisation

Two polymorphs of $Cy_3PAu[SC(OEt)=N(C_6H_4Cl\text{-}3)]$, **1**, have been characterised after recrystallisation by slow evaporation at room temperature, namely, a triclinic form ($P\bar{1}$ with $Z' = 1$; from ethanol) and a monoclinic form ($P2_1/c$; $Z' = 1$; from acetonitrile/dichloromethane, 1:1 v/v); the polymorphs are labelled the **α**- and **β**-forms, respectively. Recrystallisation experiments of **1** from acetonitrile/chloroform (1:1 v/v), acetonitrile/dichloromethane (1:1 v/v), dichloromethane/ethanol (1:1 v/v), dichloromethane/isopropanol (1:1 v/v), chloroform/ethanol (1:1 v/v) and ethanol solutions were conducted. The measured PXRD patterns indicated the **β**-form was obtained exclusively except from ethanol solution, which yielded the **α**-form only.

The IR spectra of the **α**- and **β**-forms of **1** show no significant differences and reveal the presence of characteristic thiocarbamato bands at 1,577, 1,149 and 1,087 cm^{-1}, which correspond to the stretching vibrations of the ν(C=N), ν(C–O) and ν(C–S) bonds, respectively.

Compound **1** is anticipated to undergo complete relaxation in $CDCl_3$ solution, leading to uniform NMR characteristics for both polymorphs. Indeed, the spectra were identical and exhibited the expected resonances and integration in the ^1H NMR spectrum. The notable feature of the $^{13}C\{^1H\}$ NMR spectrum is the most shielded resonance at 165.5 ppm due to the quaternary carbon of the thiocarbamato ligand.

The luminescence profiles of the **α**- and **β**-forms of **1** were investigated in the solid-state at 77 K. Each polymorphic form displayed similar excitation spectra but with an opposite pattern of peak maxima, Table 2 and Figure 2. Thus, λ_{max} was 301 nm for the **α**-form while for the **β**-form, λ_{max} was the high energy peak at 264 nm. The low intensity peaks were at λ = 271 and 295 nm for the **α**- and **β**-forms, respectively. Despite the distinct excitation spectra, in both cases, the **α**-and **β**-forms exhibited emission profiles that peaked at around 600 nm, see Figure 2. The low-energy emissions at approximately 600 nm are attributed to thiolate-to-gold ligand-to-metal charge transfer (LMCT) transitions.[98] This assignment is supported by the expectation that thiolate-to-phosphine ligand-to-ligand charge transfer (LLCT) transitions would occur at higher energies.[98]

Table 2: Solid-state luminescence data for the **α**- and **β**-forms of **1**.

Compound	λ (excitation; nm)	λ (emisson; nm)	Relative intensity
α-form	301		924
	271		517
		609	942
β-form	295		407
	264		489
		603	502

Based on the calculated UV spectrum, the absorption peak at 301 nm observed for the **α**-form arises from the HOMO to LUMO +1 transition, due to the excitation of a π-electron of the thiocarbamato ligand to the *d* orbital of the gold centre. On the other hand, the absorption peak at 264 nm in the experimental excitation spectrum of the **β**-form is due to the HOMO to LUMO + 2 transition. The transitions are shown in the spatial plots of Figure 3.

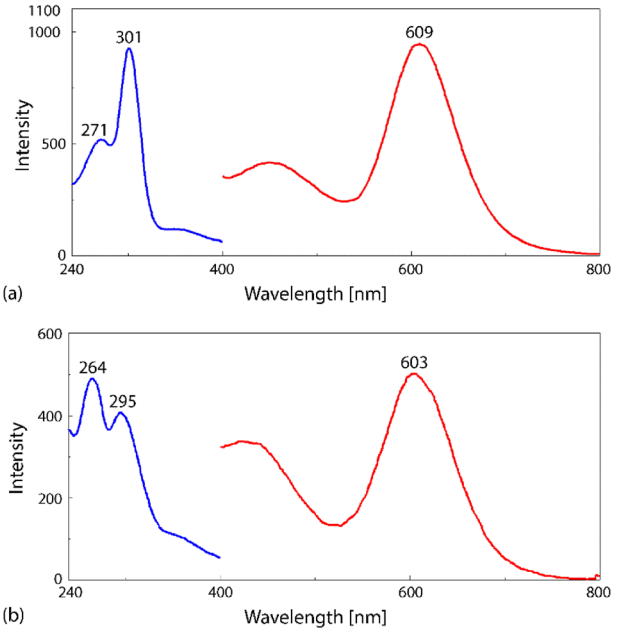

Figure 2: Solid-state excitation (blue trace) and emission (red trace) spectra measured at 77 K for the (a) **α**-form (λ_{ex} = 301 nm) and (b) **β**-form (λ_{ex} = 264 nm).

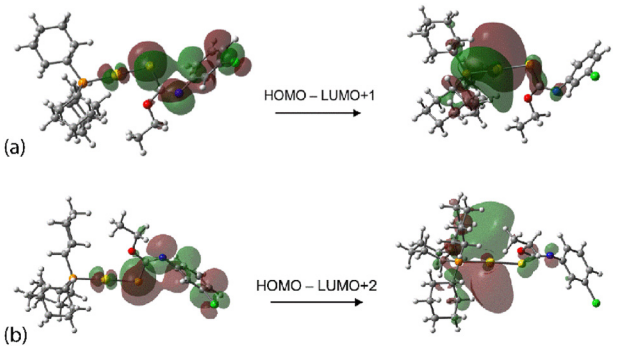

Figure 3: Spatial plots (isovalue = 0.03 a.u.) of selected molecular orbitals for the (a) **α**-form and (b) **β**-form calculated for each optimised ground state geometry.

3.2 Molecular structures

While to a first approximation the molecular structures in the **α**- and **β**-forms of **1** are similar, notable conformational differences are apparent from the molecular structure diagrams illustrated in Figure 4; key geometric parameters are collected in Table 3. For each polymorph, the gold atom is linearly coordinated by sulphur and phosphorus atoms. The free ligand, that is, $S=C(OEt)N(H)C_6H_4Cl\text{-}3$, is available for comparison of key geometric parameters.[99] The lengthening and shortening of the C1–S1 and C1–N1 bond lengths of 1.6676(16) and 1.340(2) Å, respectively, compared with those in the **α**- and **β**-forms of **1** is particularly noteworthy as are the angles subtended at the quaternary-C1 atom. Specifically, the angles subtended at the C1 atom by the doubly-bonded N1 atom are systematically wider than those of the free ligand, that is, S1–C1–N1 = 122.27(11)° and O1–C1–N1 = 113.07(13)°, and concomitant reduction in the S1–C1–O1 angle, 124.66(11)°.[99] These data confirm the S1 atoms in the **α**- and **β**-forms are coordinating the gold atom as thiolato-S atoms.

The bond lengths involving the sulphur and phosphorus atoms represent the major geometric differences between the molecules; as per normally observed, the Au–S1 bond length is longer than the Au–P1 bond. The Au–S1 bond length in the **α**-form [2.2971(6) Å] is shorter than the equivalent bond in the **β**-form [2.3157(7) Å], and a similar trend is evident in the Au–P1 bond lengths although not as pronounced, that is, 2.2667(6) compared with 2.2704(7) Å. These trends are clearly related to the close approach of the ethoxy-O atom to the gold centre which is shorter by approximately 0.06 Å in the **β**-form, Table 3; a further reason for the relative elongation of the Au–S1 bond in the **α**-form might relate to the participation of the thiolato-S1 atom in a close intermolecular contact, as discussed below.

The central CNOS residue is strictly planar exhibiting a r.m.s. deviations of 0.0006 and 0.0070 Å for the **α**- and **β**-forms, respectively. While this planarity generally extends to the ethoxy groups, kinks, in opposite orientations, of up to 20° are noted in the C1–N1–C2–C3 and C1–N1–C2–C7 torsion angles, Table 3. These differences between molecules notwithstanding, as evident from Figure 4c and d, rather large conformational disparities are apparent. In Figure 4c, the cyclohexyl groups of the two molecules have been overlaid resulting in very distinct relative orientations for the thiocarbamato residues, as reflected in a difference of approximately 43° in the P1–Au–S1–C1 torsion angles. When the thiocarbamato residues are overlaid, Figure 4d, the

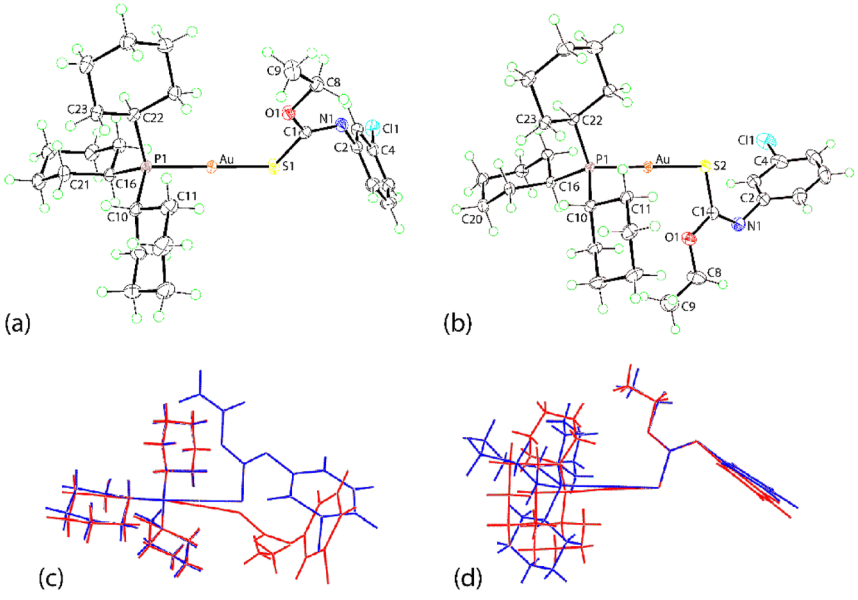

Figure 4: Molecular structures of the (a) **α**-form and (b) **β**-form of **1** showing atom labelling schemes and 50 % displacement ellipsoids, and overlay diagrams of the **α**- (red image) and **β**-forms (blue image) overlapped so that the (c) cyclohexyl groups are coincident and (d) the thiocarbamato residues are coincident.

Table 3: Selected bond lengths (Å) and angles (°) for the **α**- and **β**-forms of **1**.

Parameter	α-form	β-form	Parameter	α-form	β-form
Au–S1	2.2971(6)	2.3157(7)	Au–S1–C1–N1	−179.91(19)	174.9(3)
Au–P1	2.2667(6)	2.2704(7)	S1–C1–O1–C8	175.39(16)	−176.6(2)
Au···O1	3.1552(17)	3.097(2)	S1–C1–N1–C2	−3.1(3)	−1.1(5)
C1–S1	1.752(2)	1.757(3)	P1–Au–S1–C1	135.0(4)	91.7(17)
C1–O1	1.351(3)	1.346(4)	C1–O1–C8–C9	−170.6(2)	174.2(3)
C1–N1	1.276(3)	1.273(4)	C1–N1–C2–C3	101.7(3)	−84.7(4)
C2–N1	1.415(3)	1.409(4)	C1–N1–C2–C7	−82.2(3)	101.9(4)
P1–Au–S1	176.431(19)	178.96(3)	Au–P1–C10–C11	54.05(18)	57.0(2)
Au–S1–C1	107.19(8)	105.11(10)	Au–P1–C10–C15	−67.86(18)	−65.2(2)
S1–C1–O1	115.03(17)	114.5(2)	Au–P1–C16–C17	−51.16(17)	−60.6(2)
S1–C1–N1	124.37(18)	125.8(2)	Au–P1–C16–C21	−177.23(15)	172.45(18)
O1–C1–N1	120.6(2)	119.6(3)	Au–P1–C22–C23	−155.36(15)	−150.40(17)
Au–S1–C1–O1	−0.12(18)	−7.4(2)	Au–P1–C22–C27	−28.20(18)	−23.9(2)

cyclohexyl residues in the polymorphs are rotated by approximately 60° with respect to each other.

Density functional theory (DFT) calculations were performed on the **α**- and **β**-forms at the M06 level of theory. Preliminary calculations show both **α**- and **β**-forms are isoenergetic based on single-point calculations with the energy calculated for the **α**-form computing to 433.78 eV compared with 433.79 eV for the **β**-form.

This conclusion was confirmed by an evaluation of the isomerisation kinetics between the **α**- and **β**-forms. Specifically, the Au–S1 bond rotation kinetics were calculated by using constrained structural optimisation at different P1–Au–S1–C1 dihedral angles. The rotation about the Au–S1 bond in each of the **α**- and **β**-forms of **1** is effectively barrierless, as illustrated for the **α**-form in Figure 5.

3.3 Molecular packing

The analysis of the molecular packing was initially conducted based on geometric considerations[94] followed by an analysis of surface contacts; the geometric parameters characterising the identified intermolecular contacts in the crystals are listed in Table 4. Two short contacts were detected for the **α**-form, namely cyclohexyl-C–H···S(thiolate) and methyl-C–H···π(chlorophenyl) contacts which occur between molecules aligned along the *a*-axis as shown in Figure 6a. The chains pack without directional interactions between them; a view of the unit-cell contents is shown in Figure 6b.

Table 4: Geometric parameters characterising the specified intermolecular contacts in the crystals of the **α**- and **β**-forms of **1**.

A	H	B	H···B	A···B	A–H···B	Symmetry Operation
α-form						
C17	H17a	S1	2.86	3.760(3)	152	$1+x, y, z$
C9	H9c	Cg(C2–C7)	2.92	3.764(3)	145	$-x, 1-y, 1-z$
β-form						
C20	H20a	Cg(C2–C7)	2.77	3.755(4)	172	$1-x, 1-y, 1-z$
Cg(C2–C7)	–	Cg(C2–C7)	–	3.934(2)	0[a]	$1-x, 1-y, -z$

[a]angle between the aromatic rings.

A distinct mode of packing is noted for the crystal of the **β**-form of **1**. In this case, methyl-C–H···π(chlorophenyl) and π(chlorophenyl)···π(chlorophenyl) contacts are apparent, each occurring between centrosymmetrically related molecules aligned along the *c*-axis. The slippage between the parallel chlorophenyl rings involved in the π···π interaction is 2.15 Å with the result that the closest C···C contact within the pair of participating rings of 3.370(5) Å occurs between C5 atoms [symmetry operation: $1-x, 1-y, -z$]. A view of the supramolecular chain featuring these contacts is shown in

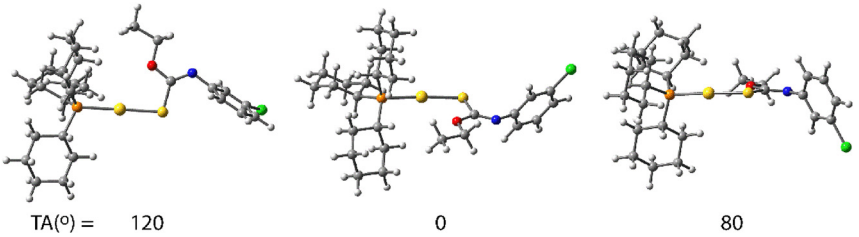

Figure 5: The relative enthalpies calculated for the **α**-form at P1–Au–S1–C1 torsion angles (TA) of 120, 0 and 80°. Regardless of the value of the torsion angle, the enthalpy computes to 0 kJ/mol.

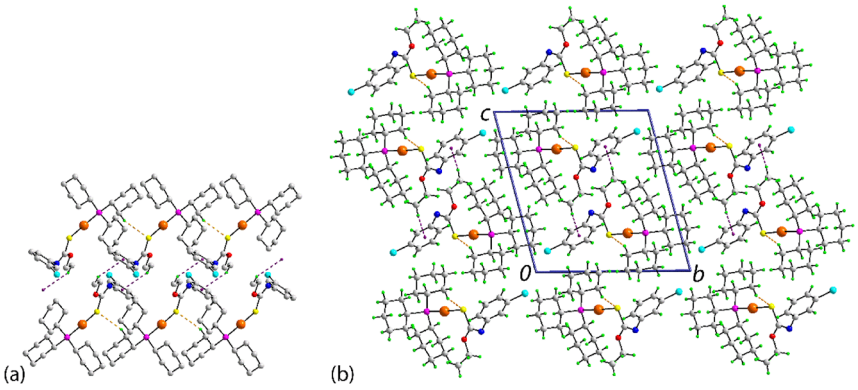

Figure 6: Supramolecular association in the crystal of the **α**-form of **1**: (a) Supramolecular chain along the *a*-axis and (b) view of the unit-cell contents shown in projection down the *a*-axis. The cyclohexyl-C–H···S(thiolate) and methyl-C–H···π(chlorophenyl) contacts are shown as orange and purple dashed lines, respectively. In (a), the non-participating H atoms have been omitted.

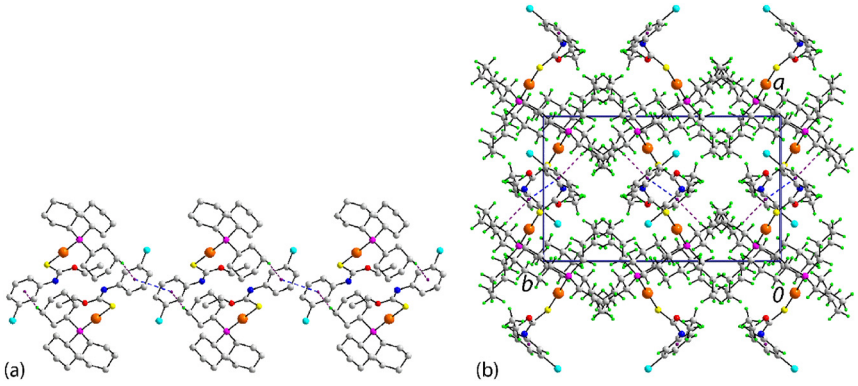

Figure 7: Supramolecular association in the crystal of the **β**-form of **1**: (a) Supramolecular chain along the *c*-axis and (b) view of the unit-cell contents shown in projection down the *c*-axis. The methyl-C–H···π(chlorophenyl) and π(chlorophenyl)···π(chlorophenyl) contacts are shown as purple and blue dashed lines, respectively. In (a), the non-participating H atoms have been omitted.

Figure 7a. No directional interactions are noted between the chains with the unit-cell contents illustrated in Figure 7b.

3.4 Hirshfeld surface analysis

The delineation of the molecular surface interactions participating in molecular packing of the **α**- and **β**-forms of **1** was carried out by generating Hirshfeld surfaces mapped over normalised contact distances, d_{norm},[100] and two-dimensional fingerprint plots[101] using Crystal Explorer 21[102] and standard protocols.[103] In these analyses, the C–H bond lengths were adjusted to their neutron values (1.08 Å).

The analysis of the calculated surface contacts in the **α**- and **β**-forms of **1** reveal remarkable similarities in the predominant interactions, Figure 8. Primarily, the overall two-dimensional fingerprint plots for each crystal present very similar distributions, Figure 8a. This is highlighted

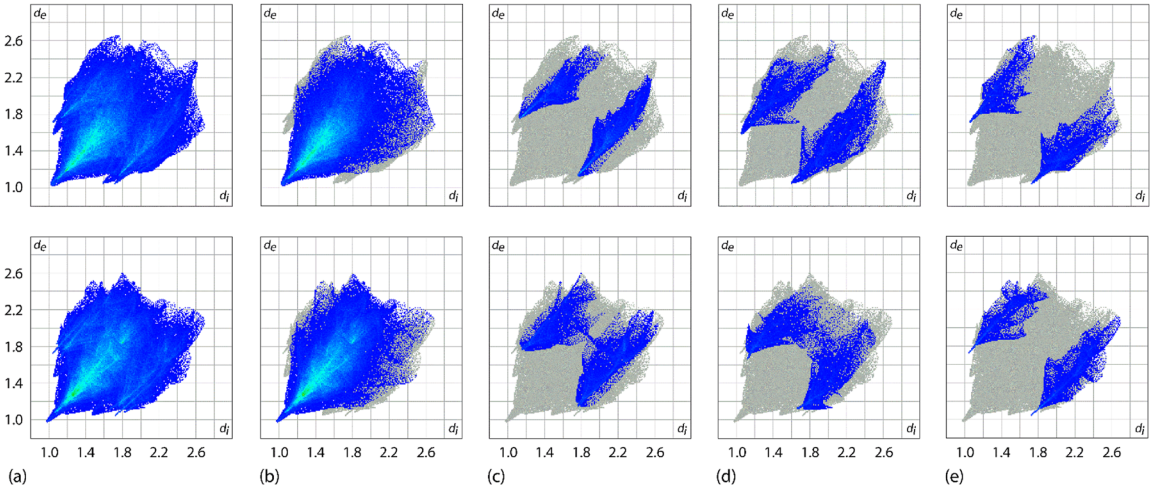

Figure 8: Two-dimensional fingerprint plots: (a) overall and those delineated into (b) H···H, (c) Cl···H/H···Cl, (d) C···H/H···C and (e) S···H/H···S contacts for the **α**-form (upper view) and **β**-form.

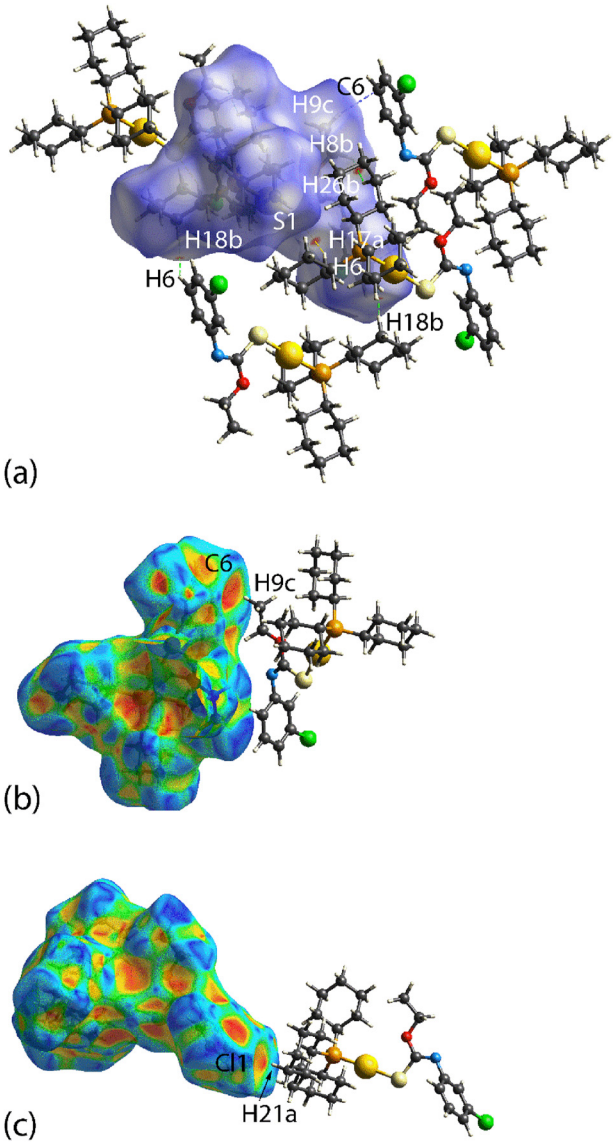

Figure 9: Views of the hirshfeld surface of the **α**-form mapped of **1** over (a) d_{norm} in the range −0.0932 to 1.5942 arbitrary units highlighting cyclohexyl-C17–H17a···S1, ethoxy-methylene-C8–H8b···H26b–C26(methylene-cyclohexyl), cyclohexyl-methylene-C18–H18b···H6–C6(π-chlorophenyl) and ethoxy-methyl-C9–H9c···C6(chlorophenyl) contacts as red spots, and the shape-index property highlighting (b) cyclohexyl-C9–H9c···π(C6) and (c) cyclohexyl-C21–H21a···Cl1 contacts.

by the observation and the H···H interactions account for 67.8 % of all surface contacts in each crystal and which also reflects the absence of strong, directional interactions in the molecular packing, Figure 8b. Other significant contacts include Cl···H/H···Cl interactions, accounting for approximately 10.5 and 9.8 %, respectively, followed by C···H/H···C interactions (9.4 and 8.2 %) and S···H/H···S contacts (6.5 and 6.9 %) contacts, see Figure 8c–e. More information concerning the supramolecular packing is apparent in the Hirshfeld surface mapping over d_{norm}.

For the **α**-form, a red spot discerned on the Hirshfeld surface mapped over d_{norm} highlights the directional interaction noted earlier, that is, the cyclohexyl-C17–H17a···S1 contact (distance: 2.77 Å), as well as red regions corresponding to a short ethoxy-methylene-H···H(methylene-cyclohexyl), that is, C8–H8b···H26b–C26 (2.08 Å), and a cyclohexyl-methylene-H···H(π-chlorophenyl), that is, C18–H18b···H6–C6 (2.09 Å) contact; Figure 9a. The fourth red spot evident on the d_{norm}-map is attributable to an ethoxy-methyl-H···C(π-chlorophenyl) contact, that is, C9–H9c···C6 (2.66 Å). This latter interaction was also identified in the geometric analysis of the molecular packing, as C9–H9c···π(C2–C7), and is clearly indicated on the shape-index property, Figure 9b. The C9–H9c···C6 contact represents a localised C9–H9c···π(C6) interaction as opposed to a delocalised C9–H9c···π(C2–C7) interaction.[104] This is confirmed by an analysis of the remaining H9c···C-ring separations which reveals a range of

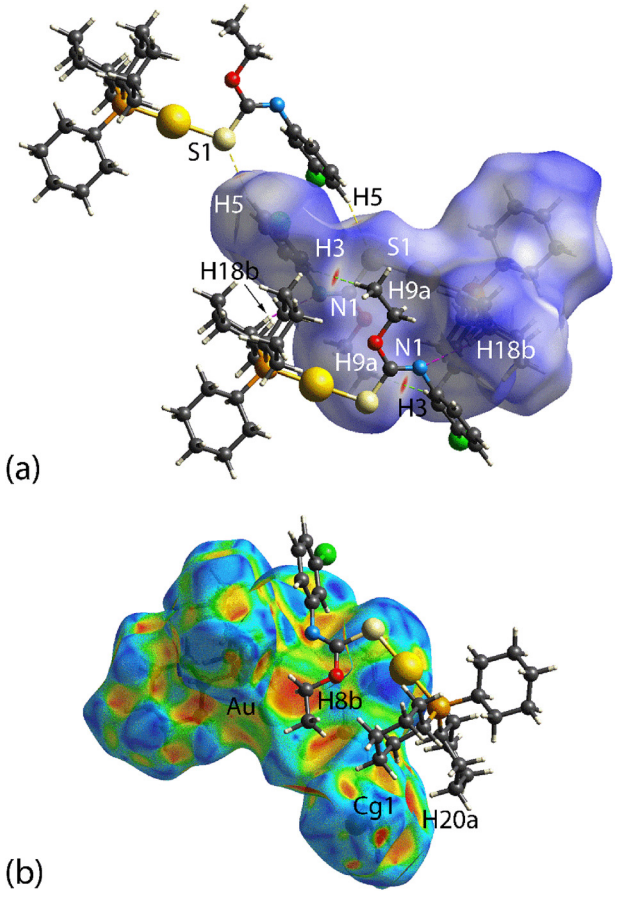

Figure 10: View of the hirshfeld surface of the **β**-form of **1** mapped over (a) d_{norm} in the range −0.1802 to 1.5756 arbitrary units highlighting cyclohexyl-C5–H5···S1, (chlorophenyl)C3–H3···H9a–C9(methyl-ethoxy) and N1···H18b–C18(methylene-cyclohexyl) contacts and (b) shape-index property highlighting cyclohexyl-C20–H20a···π(C2–C7) (=Cg1) and ethoxy-methylene-C8–H8b···Au contacts.

separations from 2.83 Å (H9c···C7) to 3.59 Å (H9c···C3), that is, an asymmetric distribution substantiating the significance of the C9–H9c···π(C6) contact. The other apparent contact not identified in the above geometric analysis is indicated in Figure 9c, namely a contact involving the chlorine atom, that is, cyclohexyl-C21–H21a···Cl1 (2.92 Å).

For the **β**-form of **1**, the d_{norm} surface plot shown in Figure 10a reveals the presence of additional contacts not identified in the conventional analysis of the molecular packing, namely long chlorophenyl-C5–H5···S1 (2.79 A) and chlorophenyl-C3–H3···H9a–C9(methyl-ethoxy) (1.98 Å) contacts. Also discerned in Figure 10a, is a faint red spot attributed to a N1···H18b–C18(methylene-cyclohexyl) contact of 2.55 Å. The shape-index plot highlights the presence of cyclohexyl-C20–H20a···π(C2–C7) interactions which occur between centrosymmetrically related molecules, Figure 10c, as identified in the above geometric analysis. More interesting is a prominent feature between the ethoxy-methylene-C8–H8b and gold atoms (2.94 Å). Such Au···H contacts have attracted interest in the recent literature, especially in relation to gold-catalysis.[105–107]

4 Conclusions

Two polymorphs have been characterised for $Cy_3PAu[SC(OEt)=N(C_6H_4Cl\text{-}3)]$ which differ in the conformations in each of the thiocarbamato and cyclohexylphosphane residues. Computational chemistry confirms the molecules are isoenergetic and to have practically a zero barrier to interconversion about the Au–S bond. Clearly, there is a subtle, solvent-dependent interplay between the adopted conformation in the crystal and the prevalence of cyclohexyl-C–H···S(thiolate) and methyl-C–H···π(chlorophenyl) contacts in the **α**-form (isolated exclusively from ethanol solution), and methyl-C–H···π(chlorophenyl) and π(chlorophenyl)···π(chlorophenyl) contacts in the packing of the **β**-form (isolated from different solvent systems other than ethanol).

Research ethics: Not applicable.
Informed consent: Not applicable.
Author contributions: All authors have accepted responsibility for the entire content of this manuscript and approved its submission. Chien Ing Yeo: Synthesis, Spectroscopy, Formal analaysis, Writing – review & editing. Yee Seng Tan: X-ray data collection, PXRD, Formal analysis, Writing – review & editing. Wai Kit Tang: Computational chemisty, Formal analysis, Writing – review and editing. Edward R. T. Tiekink: Conceptulisation, Crystallography, Formal analysis, Writing – review & editing.
Conflict of interests: The authors state no conflict of interest.
Use of Large Language Models, AI and Machine Learning Tools: None declared.
Research funding: None declared.
Data availability: Not applicable.

References

1. Yeo, C. I.; Ooi, K. K.; Akim, A. M.; Ang, K. P.; Fairuz, Z. A.; Halim, S. N. B. A.; Ng, S. W.; Seng, H.-L.; Tiekink, E. R. T. The Influence of R Substituents in Triphenylphosphinegold(I) Carbonimidothioates, $Ph_3PAu[SC(OR)=NPh]$ (R = Me, Et and iPr), upon In Vitro Cytotoxicity against the HT-29 Colon Cancer Cell Line and upon Apoptotic Pathways. *J. Inorg. Biochem.* **2013**, *127*, 24–38.
2. Ooi, K. K.; Yeo, C. I.; Ang, K.-P.; Akim, A. M.; Cheah, Y.-K.; Halim, S. N. A.; Seng, H.-L.; Tiekink, E. R. T. Phosphanegold(I) Thiolates, $Ph_3PAu[SC(OR)=NC_6H_4Me\text{-}4]$ for R = Me, Et and iPr, Induce Apoptosis, Cell Cycle Arrest and Inhibit Cell Invasion of HT-29 Colon Cancer Cells through Modulation of the Nuclear Factor-κB Activation Pathway and Ubiquitination. *J. Biol. Inorg. Chem.* **2015**, *20*, 855–873.
3. Ooi, K. K.; Yeo, C. I.; Mahandaran, T.; Ang, K. P.; Akim, A. M.; Cheah, Y.-K.; Seng, H.-L.; Tiekink, E. R. T. G_2/M Cell Cycle Arrest on HT-29 Cancer Cells and Toxicity Assessment of Triphenylphosphanegold(I) Carbonimidothioates, $Ph_3PAu[SC(OR)=NPh]$, R = Me, Et, and iPr, during Zebrafish Development. *J. Inorg. Biochem.* **2017**, *166*, 173–181.
4. Yeo, C. I.; Sim, J.-H.; Khoo, C.-H.; Goh, Z.-J.; Ang, K.-P.; Cheah, Y.-K.; Fairuz, Z. A.; Halim, S. N. B. A.; Ng, S. W.; Seng, H.-L.; Tiekink, E. R. T. Pathogenic Gram-Positive Bacteria Are Highly Sensitive to triphenylphosphanegold(*O*-Alkylthiocarbamates), $Ph_3PAu[SC(OR)=N(p\text{-tolyl})]$ (R = Me, Et and iPr). *Gold Bull* **2013**, *46*, 145–152.
5. Siddiqui, R.; Abjani, F.; Yeo, C. I.; Tiekink, E. R. T.; Khan, N. A. The Effects of Phosphanegold(I) Thiolates on the Biological Properties of *Acanthamoeba Castellanii* Belonging to the T4 Genotype. *J. Negat. Results Biomed.* **2017**, *16*, 6.
6. Ho, S. Y.; Tiekink, E. R. T. Supramolecular Aggregation Patterns in the Crystal Structures of the Dinuclear Phosphinegold(I) Thiolates, $[(Ph_2P(CH_2)_4PPh_2)\{AuSC(OR)=NC_6H_4Y\text{-}4\}_2]$ for *R* = Me, Et & iPr and Y = H, NO_2 & Me: The Influence on Intermolecular Interactions Exerted by *R* and Y. *CrystEngComm* **2007**, *9*, 368–378.
7. Kuan, F. S.; Ho, S. Y.; Tadbuppa, P. P.; Tiekink, E. R. T. Electronic and Steric Control over Au···Au, C–H···O and C–H···π Interactions in the Crystal Structures of Mononuclear Triarylphosphinegold(I) Carbonimidothioates: $R_3PAu[SC(OMe)=NR']$ for *R* = Ph, *O*-Tol, *M*-Tol or *P*-Tol, and *R'* = Ph, *O*-Tol, *M*-Tol, *P*-Tol or $C_6H_4NO_2$-4. *CrystEngComm* **2008**, *10*, 548–564.
8. Ho, S. Y.; Cheng, E. C.-C.; Tiekink, E. R. T.; Yam, V. W.-W. Luminescent Phosphine Gold(I) Thiolates: Correlation between Crystal Structure and Photoluminescent Properties in $[R_3PAu\{SC(OMe)=NC_6H_4NO_2\text{-}4\}]$ (R = Et, Cy, Ph) and $[(Ph_2P\text{-}R\text{-}PPh_2)\{AuSC(OMe)=NC_6H_4NO_2\text{-}4\}_2]$ (R = CH_2, $(CH_2)_2$, $(CH_2)_3$, $(CH_2)_4$, Fc). *Inorg. Chem.* **2006**, *45*, 8165–8174.
9. Bernstein, J.; Hagler, A. T. Conformational Polymorphism. The Influence of Crystal Structure on Molecular Conformation. *J. Am. Chem. Soc.* **1978**, *100*, 673–681.
10. Serezhkin, V. N.; Serezhkina, L. B. New Criterion for Conformational Polymorphism. *Crystallogr. Rep.* **2012**, *57*, 33–42.

11. Nangia, A. Conformational Polymorphism in Organic Crystals. *Acc. Chem. Res.* **2008**, *41*, 595–604.
12. Cruz-Cabeza, A. J.; Bernstein, J. Conformational Polymorphism. *Chem. Rev.* **2014**, *114*, 2170–2191.
13. Hilfiker, R., Ed. In *Polymorphism: In the Pharmaceutical Industry*; Wiley-VCH Verlag GmbH & Co. KGaA: Weinheim, Germany, 2006.
14. Brittain, H. G. *Polymorphism in Pharmaceutical Solids*, 2nd ed.; Informa Healthcare: New York NY, 2009.
15. Kitamura, M. Strategy for Control of Crystallization of Polymorphs. *CrystEngComm* **2009**, *11*, 949–964.
16. Bernstein, J. Polymorphism – A Perspective. *Cryst. Growth Des.* **2011**, *11*, 632–650.
17. Brog, J.-P.; Chanez, C.-L.; Crochet, A.; Fromm, K. M. Polymorphism, what it Is and How to Identify it: A Systematic Review. *RSC Adv*. **2013**, *3*, 16905–16931.
18. Cruz-Cabeza, A. J.; Reutzel-Edens, S. M.; Bernstein, J. Facts and Fictions about Polymorphism. *Chem. Soc. Rev.* **2015**, *44*, 8619–8635.
19. Bernstein, J. *Polymorphism in Molecular Crystals*, 2nd ed.; Oxford University Press: New York NY, 2020.
20. Brogden, R. N.; Carmine, A. A.; Heel, R. C.; Speight, T. M.; Avery, G. S. Ranitidine: A Review of its Pharmacology and Therapeutic Use in Peptic Ulcer Disease and Other Allied Diseases. *Drugs* **1982**, *24*, 267–303.
21. Trifkovic, M.; Rohani, S.; Mirmehrabi, M. Polymorphic Generation through Solvent Selection: Ranitidine Hydrochloride. *Org. Process Res. Dev*. **2007**, *11*, 138–143.
22. Drużbicki, K.; Pajzderska, A.; Chudoba, D.; Jenczyk, J.; Jarek, M.; Mielcarek, J.; Wąsicki, J. Elucidating the Structure of Ranitidine Hydrochloride Form II: Insights from Solid-State Spectroscopy and *Ab Initio* Simulations. *Cryst. Growth Des.* **2018**, *18*, 4671–4681.
23. Dunitz, J. D.; Bernstein, J. Disappearing Polymorphs. *Acc. Chem. Res.* **1995**, *28*, 193–200.
24. Bučar, D.-K.; Lancaster, R. W.; Bernstein, J. Disappearing Polymorphs Revisited. *Angew. Chem. Int. Ed.* **2015**, *54*, 6972–6993.
25. Rai, S. K.; Tothadi, S.; Arhangelskis, M.; George, C. P.; Gonnade, R. G.; Nangia, A. K. Polymorph II of Hydroxyurea 150 Years after its First Synthesis. *CrystEngComm* **2023**, *25*, 2712–2716.
26. Lea, A. P.; Faulds, D. Ritonavir. *Drugs* **1996**, *52*, 541–546.
27. Bauer, J.; Spanton, S.; Henry, R.; Quick, J.; Dziki, W.; Porter, W.; Morris, J. Ritonavir: An Extraordinary Example of Conformational Polymorphism. *Pharm. Res.* **2001**, *18*, 859–866.
28. Morissette, S. L.; Soukasene, S.; Levinson, D.; Cima, M. J.; Almarsson, Ö. Elucidation of Crystal Form Diversity of the HIV Protease Inhibitor Ritonavir by High-Throughput Crystallization. *Proc. Natl. Acad. Sci. U.S.A.* **2003**, *100*, 2180–2184.
29. Almarsson, Ö.; Peterson, M. L.; Zaworotko, M. The A to Z of Pharmaceutical Cocrystals: A Decade of Fast-Moving New Science and Patents. *Pharm. Pat. Anal.* 2012, *1*, 313–327.
30. Lee, A. Y.; Erdemir, D.; Myerson, A. S. Crystal Polymorphism in Chemical Process Development. *Annu. Rev. Chem. Biomol. Eng.* **2011**, *2*, 259–280.
31. Anwal, J.; Zahn, D. Polymorphic Phase Transitions: Macroscopic Theory and Molecular Simulation. *Adv. Drug Deliv. Rev.* **2017**, *117*, 47–70.
32. Tandon, R.; Tandon, N.; Thapar, R. K. Patenting of Polymorphs. *Pharm. Pat. Anal.* 2018, *7*, 59–63.
33. Zhou, Y.; Wang, J.; Xiao, Y.; Wang, T.; Huang, X. The Effects of Polymorphism on Physicochemical Properties and Pharmacodynamics of Solid Drugs. *Curr. Pharm. Des.* **2018**, *24*, 2375–2382.
34. Chistyakov, D.; Sergeev, G. The Polymorphism of Drugs: New Approaches to the Synthesis of Nanostructured Polymorphs. *Pharmaceutics* **2020**, *12*, 34.
35. Thakur, T. S.; Thakuria, R. Crystalline Multicomponent Solids: An Alternative for Addressing the Hygroscopicity Issue in Pharmaceutical Materials. *Cryst. Growth Des.* **2020**, *20*, 6245–6265.
36. Bolla, G.; Sarma, B.; Nangia, A. K. Crystal Engineering of Pharmaceutical Cocrystals in the Discovery and Development of Improved Drugs. *Chem. Rev.* **2022**, *122*, 11514–11603.
37. Shi, Q.; Chen, H.; Wang, Y.; Xu, J.; Liu, Z.; Zhang, C. Recent Advances in Drug Polymorphs: Aspects of Pharmaceutical Properties and Selective Crystallization. *Int. J. Pharm.* **2022**, *611*, 121320.
38. Gavezzotti, A.; Filippini, G. Polymorphic Forms of Organic Crystals at Room Conditions: Thermodynamic and Structural Implications. *J. Am. Chem. Soc.* **1995**, *117*, 12299–12305.
39. Price, S. L. Why Don't We Find More Polymorphs? *Acta Crystallogr. Sect. B: Struct. Sci. Cryst. Eng. Mater.* **2013**, *69*, 313–328.
40. Nyman, J.; Day, G. M. Static and Lattice Vibrational Energy Differences between Polymorphs. *CrystEngComm* **2015**, *17*, 5154–5165.
41. Beran, G. J. O. Modeling Polymorphic Molecular Crystals with Electronic Structure Theory. *Chem. Rev.* **2016**, *116*, 5567–5613.
42. Dybeck, E. C.; Abraham, N. S.; Schieber, N. P.; Shirts, M. R. Capturing Entropic Contributions to Temperature-Mediated Polymorphic Transformations through Molecular Modeling. *Cryst. Growth Des.* **2017**, *17*, 1775–1787.
43. Purdum, G. E.; Telesz, N. G.; Jarolimek, K.; Ryno, S. M.; Gessner, T.; Davy, N. C.; Petty, I. I. A. J.; Zhen, Y.; Shu, Y.; Facchetti, A.; Collis, G. E.; Hu, W.; Wu, C.; Anthony, J. E.; Weitz, R. T.; Risko, C.; Loo, Y.-L. Presence of Short Intermolecular Contacts Screens for Kinetic Stability in Packing Polymorphs. *J. Am. Chem. Soc.* **2018**, *140*, 7519–7525.
44. McDonagh, D.; Skylaris, C.-K.; Day, G. M. Machine-learned Fragment-Based Energies for Crystal Structure Prediction. *J. Chem. Theory Comput.* **2019**, *15*, 2743–2758.
45. Yang, M.; Dybeck, E.; Sun, G.; Peng, C.; Samas, B.; Burger, V. M.; Zeng, Q.; Jin, Y.; Bellucci, M. A.; Liu, Y.; Zhang, P.; Ma, J.; Jiang, Y. A.; Hancock, B. C.; Wen, S.; Wood, G. P. F. Prediction of the Relative Free Energies of Drug Polymorphs above Zero Kelvin. *Cryst. Growth Des.* **2020**, *20*, 5211–5224.
46. Perlovich, G. L. Formation Thermodynamics of Two-Component Molecular Crystals: Polymorphism, Stoichiometry, and Impact of Enantiomers. *Cryst. Growth Des.* **2020**, *20*, 5526–5537.
47. Abramov, Y. A.; Sun, G.; Zeng, Q. Emerging Landscape of Computational Modeling in Pharmaceutical Development. *J. Chem. Inf. Model.* **2022**, *62*, 1160–1171.
48. Abramov, Y. A.; Iuzzolino, L.; Jin, Y.; York, G.; Chen, C.-H.; Shultz, C. S.; Yang, Z.; Chang, C.; Shi, B.; Zhou, T.; Greenwell, C.; Sekharan, S.; Lee, A. Y. Cocrystal Synthesis through Crystal Structure Prediction. *Molec. Pharm.* **2023**, *20*, 3380–3392.
49. Bernstein, J.; Davey, R. J.; Henck, J. O. Concomitant Polymorphs. *Angew. Chem. Int. Ed.* **1999**, *38*, 3440–3461.
50. Nanubolu, J. B.; Krishnan, R. K. Designing a New Cocrystal of Olanzapine Drug and Observation of Concomitant Polymorphism in a Ternary Cocrystal System. *CrystEngComm* **2017**, *19*, 355–366.
51. Jha, K. K.; Dutta, S.; Munshi, P. Concomitance, Reversibility, and Switching Ability of Centrosymmetric and Non-centrosymmetric Crystal Forms: Polymorphism in an Organic Nonlinear Optical Material. *Cryst. Growth Des.* **2018**, *18*, 1126–1135.
52. Saikia, B.; Mulvee, M. T.; Torres-Moya, I.; Sarma, B.; Steed, J. W. Drug Mimetic Organogelators for the Control of Concomitant Crystallization of Barbital and Thalidomide. *Cryst. Growth Des.* **2020**, *20*, 7989–7996.

53. Tang, W.; Gong, J.; Li, T. Kinetic Retraction at the Onset of Concomitant Crystallization and Implication on Polymorphic Formation. *Molec. Pharm.* **2022**, *19*, 2676–2680.
54. Lan, J.; Bai, Y.; Ye, Y.; XuanYuan, S.; Xie, C. Simultaneous Control of Polymorphism and Morphology via Gelatin Induction for Concomitant Systems: Case Study of Sulfathiazole. *CrystEngComm* **2022**, *24*, 4584–4592.
55. Groom, C. R.; Bruno, I. J.; Lightfoot, M. P.; Ward, S. C. The Cambridge Structural Database. *Acta Crystallogr., Sect B: Struct. Sci. Cryst. Eng. Mater.* **2016**, *72*, 171–179.
56. Bruno, I. J.; Cole, J. C.; Edgington, P. R.; Kessler, M.; Macrae, C. F.; McCabe, P.; Pearson, J.; Taylor, R. New Software for Searching the Cambridge Structural Database and Visualizing Crystal Structures. *Acta Crystallogr., Sect. B: Struct. Sci. Cryst. Eng Mater.* **2002**, *58*, 389–397.
57. Tadbuppa, P. P.; Tiekink, E. R. T. [(*Z*)-*O*-Methyl *N*-(3-chlorophenyl) thiocarbamato-κ*S*](triphenylphosphine-κ*P*)Gold(I). *Acta Crystallogr. Sect. E: Crystallogr. Commun.* **2010**, *66*, m664.
58. Yeo, C. I.; Tan, S. L.; Tiekink, E. R. T. A Monoclinic Polymorph of [(Z)-N-(3-chlorophenyl)-O-methylthiocarbamato-κS](triphenylphosphane-κP)Gold(I): Crystal Structure and Hirshfeld Surface Analysis. *Acta Crystallogr. Sect. E: Crystallogr. Commun.* **2016**, *72*, 1068–1073.
59. Fürstner, A.; Davies, P. W. Catalytic Carbophilic Activation: Catalysis by Platinum and Gold π Acids. *Angew. Chem. Int. Ed.* **2007**, *46*, 3410–3449.
60. Krause, N.; Belting, V.; Deutsch, C.; Erdsack, J.; Fan, H.-T.; Gockel, B.; Hoffmann-Röder, A.; Morita, N.; Volz, F. Golden Opportunities in Catalysis. *Pure Appl. Chem.* **2008**, *80*, 1063–1069.
61. Praveen, C. Carbophilic Activation of π-systems via Gold Coordination: Towards Regioselective Access of Intermolecular Addition Products. *Coord. Chem. Rev.* **2019**, *392*, 1–34.
62. Caracelli, I.; Zukerman-Schpector, J.; Tiekink, E. R. T. Supramolecular Synthons Based on Gold···π(arene) Interactions. *Gold Bull* **2013**, *46*, 81–89.
63. Haruta, M. Gold as a Novel Catalyst in the 21st Century: Preparation, Working Mechanism and Applications. *Gold Bull* **2004**, *37*, 27–36.
64. Hashmi, A. S. K.; Hutchings, G. J. Gold Catalysis. *Angew. Chem. Int. Ed.* **2006**, *45*, 7896–7936.
65. Nugent, W. A. "Black Swan Events" in Organic Synthesis. *Angew. Chem. Int. Ed.* **2012**, *51*, 8936–8949.
66. Gaillard, S.; Cazin, C. S. J.; Nolan, S. P. N-heterocyclic Carbene Gold(I) and Copper(I) Complexes in C–H Bond Activation. *Acc. Chem. Res.* **2012**, *45*, 778–787.
67. Hendrich, C. M.; Sekine, K.; Koshikawa, T.; Tanaka, K.; Hashmi, A. S. K. Homogeneous and Heterogeneous Gold Catalysis for Materials Science. *Chem. Rev.* **2021**, *121*, 9113–9163.
68. Wang, W.; Ji, C.-L.; Liu, K.; Zhao, C.-G.; Lia, W.; Xie, J. Dinuclear Gold Catalysis. *Chem. Soc. Rev.* **2021**, *50*, 1874–1912.
69. Legon, A. C. Tetrel, Pnictogen and Chalcogen Bonds Identified in the Gas Phase before They Had Names: A Systematic Look at Non-covalent Interactions. *Phys. Chem. Chem. Phys.* **2017**, *19*, 14884–14896.
70. Edwards, A. J.; Mackenzie, C. F.; Spackman, P. R.; Jayatilaka, D.; Spackman, M. A. Intermolecular Interactions in Molecular Crystals: What's in a Name? *Faraday Discuss.* **2017**, *203*, 93–112.
71. Schneider, H.-J. Noncovalent Interactions: A Brief Account of a Long History. *J. Phys. Org. Chem.* **2022**, *35*, e4340.
72. Clark, T.; Hennemann, M.; Murray, J. S.; Politzer, P. Halogen Bonding: The Sigma-Hole. *J. Mol. Model.* **2007**, *13*, 291–296.
73. Murray, J. S.; Lane, P.; Clark, T.; Politzer, P. J. σ-Hole Bonding: Molecules Containing Group VI Atoms. *Mol. Model.* **2007**, *13*, 1033–1038.
74. Kolář, M. H.; Hobza, P. Computer Modeling of Halogen Bonds and Other σ-hole Interactions. *Chem. Rev.* **2016**, *116*, 5155–5187.
75. Pandiyan, B. V.; Deepa, P.; Kolandaivel, P. Studies on the σ–hole Bonds (Halogen, Chalcogen, Pnicogen and Carbon Bonds) Based on the Orientation of Crystal Structure. *Mol. Phys.* **2016**, *114*, 3629–3642.
76. Politzer, P.; Murray, J. S. σ-Hole Interactions: Perspectives and Misconceptions. *Crystals* **2017**, *7*, 212.
77. Politzer, P.; Murray, J. S.; Clark, T.; Resnati, G. The σ-hole Revisited. *Phys. Chem. Chem. Phys.* **2017**, *19*, 32166–32178.
78. Murray, J. S.; Politzer, P. Interaction and Polarization Energy Relationships in σ-hole and π-hole Bonding. *Crystals* **2020**, *10*, 76.
79. Bauzá, A.; Frontera, A. σ/π-Hole Noble Gas Bonding Interactions: Insights from Theory and Experiment. *Coord. Chem. Rev.* **2020**, *404*, 213112.
80. Stenlid, J. H.; Johansson, A. J.; Brinck, T. σ-Holes and σ-lumps Direct the Lewis Basic and Acidic Interactions of Noble Metal Nanoparticles: Introducing Regium Bonds. *Phys. Chem. Chem. Phys.* **2018**, *20*, 2676–2692.
81. Frontera, A.; Bauzá, A. Regium–π Bonds: An Unexplored Link between Noble Metal Nanoparticles and Aromatic Surfaces. *Chem. – Eur. J.* **2018**, *24*, 7228–7234.
82. Piña, M. N. P.; Frontera, A.; Bauzá, A. Regium–π Bonds Are Involved in Protein–Gold Binding. *J. Phys. Lett* **2020**, *11*, 8259–8263.
83. Burguera, S.; Frontera, A.; Bauzá, A. Regium-π Bonds Involving Nucleobases: Theoretical Study and Biological Implications. *Inorg. Chem.* **2023**, *62*, 6740–6750.
84. Hall, V. J.; Siasios, G.; Tiekink, E. R. T. Triorganophosphinegold(I) Carbonimidothioates. *Aust. J. Chem.* **1993**, *46*, 561–570.
85. Yeo, C. I.; Tan, S. L.; Otero-de-la-Roza, A.; Tiekink, E. R. T. A Conformational Polymorph of $Ph_3PAu[SC(OEt)=NPh]$ Featuring an Intramolecular Au···π Interaction. *Z. Kristallogr.* **2016**, *231*, 653–661.
86. Yeo, C. I.; Khoo, C.-H.; Chu, W.-C.; Chen, B.-J.; Chu, P.-L.; Sim, J.-H.; Cheah, Y.-K.; Ahmad, J.; Halim, S. N. A.; Seng, H.-L.; Ng, S.; Otero-de-la-Roza, A.; Tiekink, E. R. T. The Importance of Au···π(aryl) Interactions in the Formation of Spherical Aggregates in Binuclear Phosphanegold(I) Complexes of a Bipodal Thiocarbamate Dianion: A Combined Crystallographic and Computational Study, and Anti-microbial Activity. *RSC Adv.* **2015**, *5*, 41401–41411.
87. Kuan, F. S.; Jotani, M. M.; Tiekink, E. R. T. New Monoclinic Form of {O-Ethyl N-(4-nitrophenyl)thiocarbamato-κS}(tri-4-tolylphosphane-κP) Gold(I): Crystal Structure and Hirshfeld Surface Analysis. *Acta Crystallogr. Sect. E: Crystallogr. Commun.* **2017**, *73*, 1465–1471.
88. Broker, G. A.; Tiekink, E. R. T. [*O*-Ethyl *N*-(4-nitrophenyl)thiocarbamato-κS](tri-*p*-tolylphosphine-κP)Gold(I). *Acta Crystallogr. Sect. E: Crystallogr. Commun.* **2008**, *64*, m1582.
89. Rigaku Oxford Diffraction, CrysAlis PRO; Oxfordshire, England, 2017.
90. Sheldrick, G. M. A Short History of SHELX, *Acta Crystallogr. Sect. A: Found. Crystallogr.* **2008**, *64*, 112–122.
91. Sheldrick, G. M. Crystal Structure Refinement with SHELX. *Acta Crystallogr. Sect. C: Struct. Chem.* **2015**, *71*, 3–8.
92. Farrugia, L. J. WinGX and ORTEP for Windows: An Update. *J. Appl. Crystallogr.* **2012**, *45*, 849–854.
93. Brandenburg, K.; *Diamond, Crystal Impact GbR*: Bonn, Germany, 2006.
94. Spek, A. L. checkCIF Validation Alerts: What They Mean and How to Respond. *Acta Crystallogr. Sect. E: Crystallogr. Commun.* **2020**, *76*, 1–11.
95. Zhao, Y.; Truhlar, D. G. The M06 Suite of Density Functionals for Main Group Thermochemistry, Thermochemical Kinetics, Noncovalent Interactions, Excited States, and Transition Elements: Two New Functionals and Systematic Testing of Four M06-Class Functionals and 12 Other Functionals. *Theo. Chem. Acc.* **2008**, *120*, 215–241.

96. Perdew, J. P.; Burke, K.; Ernzerhof, M. Generalized Gradient Approximation Made Simple. *Phys. Rev. Lett.* **1996**, *77*, 3865.
97. Frisch, M. J.; Trucks, G. W.; Schlegel, H. B.; Scuseria, G. E.; Robb, M. A.; Cheeseman, J. R.; Scalmani, G.; Barone, V.; Mennucci, B.; Petersson, G. A.. *Gaussian 16 Rev. B.01*: Wallingford, CT, 2016.
98. Yam, V. W.-W.; Chan, C.-L.; Cheung, K.-K. Synthesis and Photophysics of Dinuclear Gold(I) Thiolates of Bis(diphenylphosphino)-Alkyl- and -Aryl-Amines. Crystal Structure of $[Au_2\{Ph_2PN(C_6H_{11})PPh_2\}(SC_6H_4F\text{-}p)_2]$. *J. Chem. Soc., Dalton Trans.* **1996**, 4019–4022.
99. Tan, Y. S.; Yeo, C. I.; Tiekink, E. R. T. Crystal Structure of N-(3-chlorophenyl)ethoxycarbothioamide, $C_9H_{10}ClNOS$. *Z. Kristallogr. – New Cryst. Struct.* **2018**, *233*, 511–512.
100. McKinnon, J. J.; Spackman, M. A.; Mitchell, A. S. Novel Tools for Visualizing and Exploring Intermolecular Interactions in Molecular Crystals. *Acta Crystallogr. Sect. B: Struct. Sci. Cryst. Eng. Mater.* **2004**, *60*, 627–668.
101. Spackman, M. A.; McKinnon, J. J. Fingerprinting Intermolecular Interactions in Molecular Crystals. *CrystEngComm* **2002**, *4*, 378–392.
102. Spackman, P. R.; Turner, M. J.; McKinnon, J. J.; Wolff, S. K.; Grimwood, D. J.; Jayatilaka, D.; Spackman, M. A. CrystalExplorer: A Program for Hirshfeld Surface Analysis, Visualization and Quantitative Analysis of Molecular Crystals. *J. Appl. Cryst.* **2021**, *54*, 1006–1011.
103. Tan, S. L.; Jotani, M. M.; Tiekink, E. R. T. Utilizing Hirshfeld Surface Calculations, Non-covalent Interaction (NCI) Plots and the Calculation of Interaction Energies in the Analysis of Molecular Packing. *Acta Crystallogr. Sect. E: Crystallogr. Commun.* **2019**, *75*, 308–318.
104. Schollmeyer, D.; Shishkin, O. V.; Rühl, T.; Vysotsky, M. O. OH–π and Halogen–π Interactions as Driving Forces in the Crystal Organisations of Tri-bromo and Tri-iodo Trityl Alcohols. *CrystEngComm* **2008**, *10*, 715–723.
105. Schmidbaur, H.; Raubenheimer, H. G.; Dobrzańska, L. The Gold–Hydrogen Bond, Au–H, and the Hydrogen Bond to Gold, Au···H–X. *Chem. Soc. Rev.* **2014**, *43*, 345–380.
106. Darmandeh, H.; Löffler, J.; Tzouras, N. V.; Dereli, B.; Scherpf, T.; Feichtner, K.-S.; Vanden, B. S.; Van Hecke, K.; Saab, M.; Cazin, C. S. J.; Cavallo, L.; Nolan, S. P.; Gessner, V. H. Au···H–C Hydrogen Bonds as Design Principle in Gold(I) Catalysis. *Angew. Chem. Int. Ed.* **2021**, *60*, 21014–21024.
107. Sorroche, A.; Moreno, S.; Olmos, M. E.; Monge, M.; López-de-Luzuriaga, J. M. Deciphering the Primary Role of Au···H–X Hydrogen Bonding in Gold Catalysis. *Angew. Chem. Int. Ed.* **2023**, *62*, e202310314.

Supplementary Material: This article contains supplementary material (https://doi.org/10.1515/zkri-2024-0124).